ELSEVIER

cell
calcium

www.elsevier.com/locate/ceca

Optical single-channel recording by imaging Ca^{2+} flux through individual ion channels: theoretical considerations and limits to resolution

Jianwei Shuai, Ian Parker *

Department of Neurobiology and Behavior, University of California, Irvine, CA 92697-4550, USA

Abstract

Recent developments in microscopy and fluorescent indicators now make it possible to monitor the activity and localization of membrane ion channels by imaging Ca^{2+} flux through individual channels. Such optical approaches have advantages over electrophysiological single-channel techniques in that they are less invasive, provide spatial information and can simultaneously and independently monitor hundreds of channels. However, their kinetic resolution does not yet approach that of patch-clamp recordings. To help understand the processes that determine the temporal resolution and noise level of single-channel Ca^{2+} fluorescence signals (SCCaFTs), we simulated the microdomains of Ca^{2+} ions and Ca^{2+}-bound indicator dye that exist around the mouth of an open channel. Further, as an aid to development of improved optical techniques, we modeled the dependence of the amplitude and kinetics of SCCaFTs on parameters such as the imaging volume, the indicator concentration, affinity and mobility, and the presence of endogenous and exogenous Ca^{2+} buffers. The results indicate that under optimal conditions, including the use of confocal or total-internal reflection microscopy to image from sub-femtolitre volumes, SCCaFTs should resolve channel openings as brief as 1 ms with a signal-to-noise ratio >10.
© 2005 Elsevier Ltd. All rights reserved.

Keywords: Xenopus oocyte; Single-channel imaging; Calcium channels; Confocal microscopy; TIRF microscopy

1. Introduction

Improvements in fluorescence imaging technology and Ca^{2+}-sensitive probes have advanced to the point where it is now routinely possible to detect the Ca^{2+} flux through single Ca^{2+}-permeable ion channels [1–3]. Resolution of such 'fundamental' Ca^{2+} signals [4] was first achieved imaging Ca^{2+} liberation from intracellular stores through inositol trisphosphate receptors ("blips") [5] and through ryanodine receptors ("quarks") [6]. However, although these events were presumed to reflect single-channel activity based on their magnitudes and other characteristics, there was no definitive proof that this was indeed the case. Subsequent experiments in which fluorescence signals were imaged simultaneously with patch-clamp measurements of single-channel currents [7–10] thus represented an important advance, and established the utility of optical imaging as a means to monitor the functioning of single Ca^{2+}-permeable channels.

The emphasis of most studies to date has concerned the physiological relevance of the microdomains of Ca^{2+} in the cytosol around an open Ca^{2+} channel: for example, their roles in triggering Ca^{2+}-induced Ca^{2+} release from intracellular stores in cardiac muscle [10,11]; the spatio-temporal activation of Ca^{2+}-dependent K^+ channels [12]; and the mapping of channels on the plasma membrane [1,2]. A different aspect, on which we have focused [2,13–15], is the application of imaging techniques to monitor single-channel Ca^{2+} microdomains with high spatial and temporal resolution, so as to obtain single-channel recordings analogous to those obtained by electrophysiological patch-clamp techniques.

The invention of the patch-clamp technique [16] revolutionized our understanding of ion channel function by permit-

ting measurements of the currents flowing through single ion channels with sub-pA and sub-ms resolution. Nevertheless, patch-clamping has a number of drawbacks, and the development of optical modalities for monitoring single-channel activity promises a complementary approach with specific advantages. The relative advantages and limitations of optical single-channel recording have recently been reviewed [1–3]. In brief, major strengths include a parallel readout from numerous channels, the ability to map channel locations with sub-μm precision, and the fact that imaging techniques are relatively non-invasive and can monitor intracellular channels that are inaccessible to a patch-pipette. Present limitations of optical single-channel recording methods include their restriction to Ca^{2+}-permeable channels, imperfect quantification of single-channel current (Ca^{2+} flux), and poor temporal resolution as compared to patch-clamp recordings.

Several techniques have been used to image single-channel Ca^{2+} signals, including wide-field microscopy [7–9]; confocal linescan microscopy [10,13]; and total-internal reflection fluorescence (TIRF) microscopy [14]. Each has particular advantages, but none as yet approaches the kinetic resolution possible with patch-clamping. In part, this is due to instrumental limitations—such as the speed of the confocal scanner or the frame rate of the imaging camera. However, more fundamental limits are set by the very nature of the intracellular fluorescence Ca^{2+} signal itself. How rapidly does the local cytosolic free $[Ca^{2+}]$ around a channel rise and fall as the channel opens and closes? How fast can a fluorescent probe track these changes? How are the observed fluorescence signals blurred and slowed by the combined effects of diffusion and diffraction-limited imaging? To what extent does photon shot noise degrade the signal? Here, we explore these processes by using a computer model to numerically simulate the Ca^{2+} microdomains and corresponding fluorescence signals resulting from single-channel openings. Our aims are to establish the fundamental limits to resolution set by physical–chemical and optical constraints, and to guide the improvement of optical single-channel imaging methodologies by exploring how parameters such as imaging volume and probe characteristics can be 'tuned' to provide optimal resolution.

2. Nomenclature

The terminology used to describe localized cellular Ca^{2+} signals has evolved in a haphazard fashion, and the literature now holds a bestiary of at least 13 different terms for such events (summarized in [3]). Among those applied to single-channel cytosolic Ca^{2+} signals (as opposed to signals arising from concerted activity of clustered channels) are names specific for particular channel types: 'blips' for inositol trisphosphate receptors [5], 'quarks' for ryanodine receptors [6], and 'sparklets' for voltage-gated plasma membrane channels [10]; as well as the generic terms 'fundamental events' [4] and 'SCCaFTs' (single-channel Ca^{2+} fluorescence transients)

[7]. In earlier publications describing signals mediated by voltage-gated N-type channels we followed the 'sparklets' nomenclature coined by Wang et al. [10]. However, extension of our studies to include ligand-gated channels has now rendered that nomenclature inappropriate. Moreover, we feel that it is important to clearly distinguish between the Ca^{2+} microdomain itself, and its reflection as visualized (after considerable blurring by diffusion and optical diffraction) by fluorescence imaging. We have thus adopted SCCaFT (pronounced *skaft*) to refer to the resulting fluorescence signal reported by a Ca^{2+}-sensitive probe, and propose 'SCCaT' (single-channel Ca^{2+} transient: *skat*) as a generic term to refer to the local microdomain of Ca^{2+} created by the opening of a single Ca^{2+}-permeable channel.

3. Single-channel imaging modalities

3.1. Probes of channel conformation versus probes of ion flux

Two very different approaches have been taken regarding optical probes for monitoring single-channel activity. One involves genetically engineered or exogenous fluorophores that sense conformational changes in channel structure associated with gating or pore opening [17]. This method is powerful in that it can provide mechanistic insights into the molecular details of channel function, but its utility for tracking channel openings and closings with good time resolution is severely limited because only one or a few fluorophore molecules can be attached to each channel. Fluorescence signals, are therefore, weak, and the strong excitation required to evoke sufficient emitted photons raises problems of photobleaching and phototoxicity. Instead, we concentrate here on the use of fluorescent probes that sense Ca^{2+} ions that have entered the cytosol through individual plasma membrane ion channels. This approach has the great advantage of providing inherent amplification. Hundreds or thousands of Ca^{2+} ions pass through an open channel each millisecond. An appreciable fraction of these will bind to indicator molecules, each of which can then be excited to emit numerous photons.

3.2. Kinetic resolution

The temporal resolution that can be achieved by monitoring SCCaFTs depends strongly on the volume of cytosol from which the fluorescence is monitored. Channel opening and closing results in large (tens of μM) and rapid (<1 ms) changes in free $[Ca^{2+}]$ in the immediate vicinity of the channel mouth, but these become greatly damped at increasing distances from the channel. Most single-channel Ca^{2+} imaging studies [7–14] have thus employed optical techniques designed to reject out-of-focus fluorescence and monitor fluorescence from as small a volume as possible around the channel. The best temporal resolution achieved to date in this way is about 5–10 ms [15]. In contrast, Singer and colleagues

[1,7–9] have used wide-field epifluorescence microscopy, which provides little rejection of out-of-focus fluorescence and a poorer time resolution.

3.3. Estimation of Ca^{2+} current

The fluorescence magnitude of SCCaFTs cannot readily be used to calculate the local free [Ca^{2+}] (molar) or the total Ca^{2+} flux (moles) during single-channel events. One difficulty is that studies to data have used visible-wavelength indicators, such as Oregon Green and Fluo-4, which have the advantage of displaying a huge fluorescence increase on binding Ca^{2+} but cannot provide true ratiometric measurements as with fura-2. More importantly, the gradients of Ca^{2+}-bound indicator around a channel may be narrower than can be resolved by optical microscopy and change rapidly with time, so that dye calibrations based on steady-state measurements are inapplicable. The amplitudes of SCCaFTs are thus heavily influenced by poorly known parameters such as the microscope point-spread function (p.s.f.), whether or not the event is captured in focus, and the binding kinetics of the indicator and endogenous cellular Ca^{2+} buffers. To circumvent this problem, we introduced the concept of 'signal mass' [18], representing an integral of the Ca^{2+} dependent fluorescence throughout a cellular volume sufficiently large to capture the entire signal. The rate of rise of the SCCaFT signal mass is expected to be directly proportional to the underlying Ca^{2+} current, and its peak proportional to the total Ca^{2+} influx [8,9,12,18,19]. The signal mass approach was originally applied to linescan confocal images by extrapolating the integral of the one-dimensional data to three spatial dimensions [18,19], but was later adapted to wide-field images [1,7–9]. In the latter case fluorescence is captured from the entire thickness of the cell, so that calculation of the signal mass involves no more than summing the fluorescence increase over all pixels. The rate of rise of signal mass obtained in this way provides a good measure of underlying Ca^{2+} current, irrespective of whether the event is in sharp focus [9].

4. Numerical modeling of SCCaTs and SCCaFTs

As an aid to developing appropriate technology to visualize SCCaTs and interpret the resulting fluorescence images we describe here a mathematical model to simulate the expected kinetics and spatial distribution of Ca^{2+} and Ca^{2+}-bound indicator in the cytosol adjacent to a plasma membrane Ca^{2+} channel. Similar approaches have been used before to determine how the spatio-temporal profiles of free cytosolic [Ca^{2+}] may regulate cellular functions such as vesicle fusion and ion channel activation [20–23]. Different from this, we explore the spatio-temporal profiles of the Ca^{2+}-bound indicator, and the resulting fluorescence signals as they would be visualized by different modalities of light microscope.
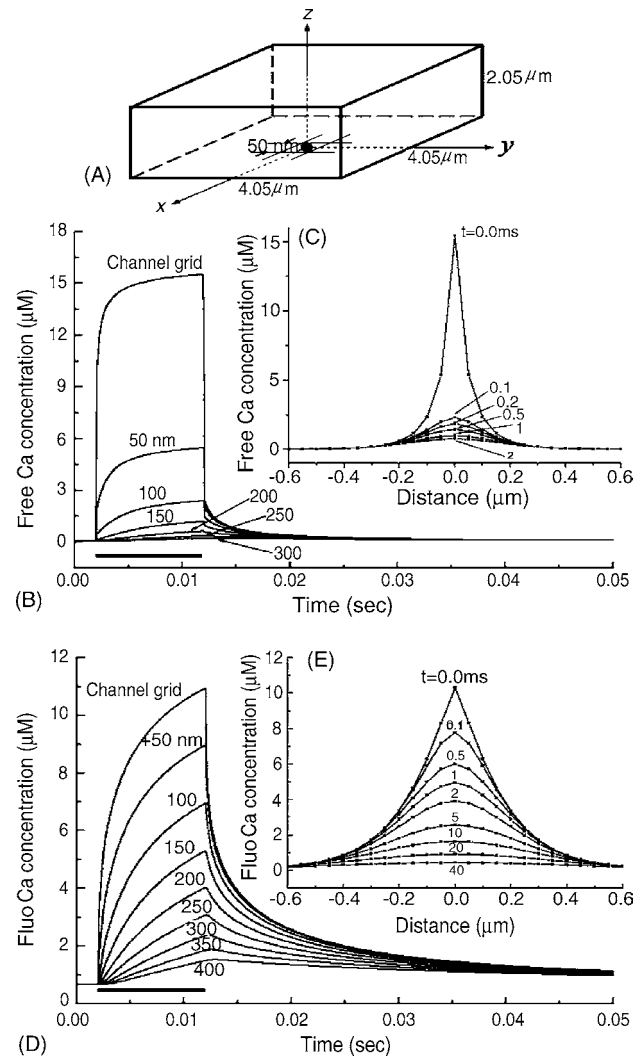

Fig. 1. Simulation of the temporal and spatial distributions of free Ca^{2+} and Ca^{2+}-bound indicator in the cytoplasm around a single plasma membrane channel, using the 'standard' parameter values listed in Table 1. (A) Sketch illustrates the geometry of the model. (B) Time course of changes in free [Ca^{2+}] measured within a 50 nm grid element centered on the channel, and in grid elements at various distances from the channel as indicated in nm. Bar marks the duration of the channel opening. (C) Spatial profiles of free [Ca^{2+}] around the channel measured just before the channel closed ($t = 0.0$), and at times of 0.1, 0.2, 0.5, 1 and 2 ms after channel closing. (D and E) Corresponding measurements of temporal and spatial profiles of [FluoCa].

4.1. The model

We simulate the propagation of Ca^{2+} throughout a cuboid cytosolic space with dimensions of $4.05 \,\mu m \times 4.05 \,\mu m \times 2.05 \,\mu m$, divided into cubic (50 nm side) grid elements (Fig. 1A). The bottom of this volume represents the plasma membrane, with a single Ca^{2+} channel located at its center (the origin of the model coordinate space). A no-flux boundary condition is applied at the plasma membrane, whereas the concentrations of all signal species are held constant at their resting levels at the other five boundaries.

Table 1
'Standard' parameter values used for simulations

Parameter	Value	Unit	Notes/references
Cytosol structure			
Height of the cytosol	2.05	μm	
Length of the cytosol	4.05	μm	
Width of the cytosol	4.05	μm	
Free Ca^{2+}			
Diffusion coefficient (D)	200	$\mu m^2\, s^{-1}$	[29]
Resting concentration $[Ca^{2+}]_{Rest}$	0.05	μM	
Fluo indicator (Fluo-4 dextran)			
Diffusion coefficient (D_{CaF})	15	$\mu m^2\, s^{-1}$	Assuming MW = 10 kD
Total concentration ($[Fluo]_T$)	40	μM	[13]
Dissociation constant (κ_F)	3.0	μM	[30]
On-rate (α_F)	150	$\mu M^{-1}\, s^{-1}$	Assumed same as Fluo-3; [25]
Off-rate (β_F)	450	s^{-1}	$\beta_F = \kappa_F \alpha_F$
Stationary buffer			
Total concentration ($[S]_T$)	300	μM	[32]
Dissociation constant ($\kappa_T = \beta_T/\alpha_T$)	2	μM	[32]
On-rate (α_S)	400	$\mu M^{-1}\, s^{-1}$	[32]
Off-rate (β_S)	800.0	s^{-1}	[32]
Exogenous mobile buffers			Present only for Fig. 10
Diffusion coefficient (D_{CaF})	200 (BAPTA), 200 EGTA)	$\mu m^2\, s^{-1}$	[31]
Dissociation constant ($\kappa_M = \beta_M/\alpha_M$)	0.16 (BAPTA), 0.15 (EGTA)	μM	[31]
On-rate (α_M)	500 (BAPTA), 5 (EGTA)	$\mu M^{-1}\, s^{-1}$	[31]
Off-rate (β_M)	80 (BAPTA), 0.75 (EGTA)	s^{-1}	[31]
Ca^{2+} channel			
Maximum Ca^{2+} current (I_{Max})	0.1	pA	[13,14]
Extracellular Ca^{2+} concentration $[Ca^{2+}]_{Ex}$	6000	μM	[13,14]

Values were taken from published literature where indicated.

The model includes the following species: cytosolic free Ca^{2+} ions, (Ca^{2+}); stationary cytosolic buffer, in free (S) and Ca^{2+}-bound forms (CaS); cytosolic Ca^{2+} indicator in free (Fluo) and Ca^{2+}-bound forms (FluoCa). FluoCa, in principle, represents any generic fluorescent Ca^{2+} indicator dye; but here we selected parameter values (Table 1) appropriate for Fluo-4 dextran, as we use this for experimental studies [13,14]. Additionally, in the case of the simulation of Fig. 10 we introduced a further mobile cytosolic buffer (M).

We consider the reactions of stationary buffer S, mobile buffer M and indicator Fluo with free Ca^{2+}:

$$[Ca^{2+}] + [X] \underset{\beta_X}{\overset{\alpha_X}{\rightleftarrows}} [CaX] \tag{1}$$

where X represents S, M or Fluo; α, forward binding rate; and β, the backward binding rate.

The reaction–diffusion equations are then described as follows: for free Ca^{2+} with diffusion coefficient D,

$$
\frac{\partial [Ca^{2+}]}{\partial t} = D\nabla^2[Ca^{2+}] + \delta_0 J_{Ch} + \beta_S[CaS]
$$
$$
- \alpha_S[Ca^{2+}]([S]_T - [CaS]) + \beta_F[FluoCa]
$$
$$
- \alpha_F[Ca^{2+}]([Fluo]_T - [FluoCa]) + \beta_M[CaM]
$$
$$
- \alpha_M[Ca^{2+}]([M]_T - [CaM]) \tag{2}
$$

in which the channel distribution function $\delta_0 = 1$ at the grid element containing the channel, otherwise $\delta_0 = 0$; for FluoCa with diffusion coefficient D_{FluoCa},

$$
\frac{\partial [FluoCa]}{\partial t} = D_{FluoCa}\nabla^2[FluoCa] + \alpha_F[Ca^{2+}]([Fluo]_T
$$
$$
- [FluoCa]) - \beta_F[FluoCa] \tag{3}
$$

for the Ca^{2+}-bound mobile buffer with diffusion coefficient D_{CaM},

$$
\frac{\partial [CaM]}{\partial t} = D_{CaM}\nabla^2[CaM]
$$
$$
+ \alpha_M[Ca^{2+}]([M]_T - [CaM]) - \beta_M[CaM] \tag{4}
$$

and for the Ca^{2+}-bound stationary buffer,

$$
\frac{\partial [CaS]}{\partial t} = \alpha_S[Ca^{2+}]([S]_T - [CaS]) - \beta_S[CaS] \tag{5}
$$

The total concentrations for Ca^{2+} indicator, mobile buffer and stationary buffer are $[Fluo]_T$, $[M]_T$ and $[S]_T$, respectively. We assume that the diffusion coefficients of the free and Ca-bound forms of the indicator and mobile buffer are equal. Thus, the concentration at any location of the free species is given by subtracting the concentrations of the Ca-bound form

from the total, and we do not explicitly consider the diffusion of free Fluo or free mobile buffer.

The channel flux is expressed as:

$$J_{Ch} = \frac{I_{Ch}}{2F\delta V} \tag{6}$$

where $F = 9.65 \times 10^{-11}$ C fmol^{-1}; δV is the small cytosolic volume around the channel pore, and the single-channel current I_{Ch} is given by:

$$I_{Ch} = \upsilon_{Ch}([Ca^{2+}]_{Ex} - [Ca^{2+}]) \tag{7}$$

where $[Ca^{2+}]_{Ex}$ is the extracellular concentration (set to 6 mM), $[Ca^{2+}]$ is the concentration at the cytosolic side of the channel and υ_{Ch} is the conductance of channel for Ca^{2+}. We define the channel current in terms of the maximum value (I_{Max}) that would flow immediately on opening of the channel which, because the resting free cytosolic $[Ca^{2+}]_{Rest}$ is negligible (50 nM), is given by:

$$I_{Max} = \upsilon_{Ch}[Ca^{2+}]_{Ex} \tag{8}$$

The resting concentrations of [FluoCa], [CaS] and [CaM] are read, respectively, as $[Fluo]_T/(1 + \kappa_F/[Ca^{2+}]_{Rest})$, $[S]_T/(1 + \kappa_S/[Ca^{2+}]_{Rest})$, and $[M]_T/(1 + \kappa_M/[Ca^{2+}]_{Rest})$; where κ_F, κ_S and κ_M are, respectively, the Ca^{2+} dissociation constants for Fluo, stationary Ca^{2+} buffer and mobile Ca^{2+} buffer.

The finite difference method was used to solve the above partial differential equations. To achieve a workable computation time (1 h to simulate 40 ms of model time with a 3 GHz Pentium) we used a time increment $\Delta t = 0.5$ μs and spatial step $\Delta x = 50$ nm, so that the cytosolic space was represented by a lattice of $81 \times 81 \times 41$ grid elements. Our principle aim was to model the distribution of [FluoCa] signals, and tests using smaller values of Δx or Δt gave similar results for this parameter. However, a spatial step of 50 nm was too coarse to accurately represent the distribution of free $[Ca^{2+}]$ close to the channel (cf. Fig. 1C).

4.2. Calculation of fluorescence signals

The model simulates the changes in [FluoCa] that occur in four dimensions (x, y, z, time) as a result of the opening of a single plasma membrane Ca^{2+} channel. To predict the resulting changes in fluorescence that would be imaged by different modes of microscopic imaging we assumed that fluorescence is linearly proportional to [FluoCa]—specifically, that free Fluo is non-fluorescent—and calculated a weighted average of [FluoCa] throughout a cytosolic volume corresponding to the microscope point-spread function (p.s.f.).

Representative p.s.f.'s of confocal and TIRF microscopes are illustrated in Fig. 5A and B. Confocal microscopy yields a p.s.f. resembling an (American) football, weighted as a Gaussian distribution in space, but with greater axial than lateral width (Fig. 5A). For the present simulations we assumed that the microscope was focused in the plane of the membrane

($z = 0$), so the resulting confocal spot would appear as one half of the 'football' shape (Fig. 5A). Then the confocal signal (Con) that would result at any point (x_0, y_0, $z_0 = 0$) can be calculated as:

$$\begin{aligned}
&\text{Con}(x_0, y_0) \\
&= \frac{1}{V_{Con}} \iiint dx\,dy\,dz [FluoCa](x, y, z) \\
&\quad \times \exp\left(-\frac{(x - x_0)^2}{\lambda_x} - \frac{(y - y_0)^2}{\lambda_y}\right) \exp\left(-\frac{z^2}{\lambda_z}\right)
\end{aligned} \tag{9}$$

with $\lambda_x = \lambda_y = 0.0325$ μm^2 and $\lambda_z = 0.231$ μm^2 chosen to match experimentally observed widths (full-width at half-maximal amplitude: FWHM) of 300 nm lateral and 800 nm in the axial dimension, and V_{Con} defined as the weighted cytosolic volume:

$$V_{Con} = \iiint dx\,dy\,dz \exp\left(-\frac{x^2}{\lambda_x} - \frac{y^2}{\lambda_y}\right) \exp\left(-\frac{z^2}{\lambda_z}\right) \tag{10}$$

The confocal signal (Con) has units of concentration: i.e. μM.

In the case of TIRFM, the p.s.f. again follows a Gaussian function in the lateral plane, but decays exponentially in the axial (z) dimension (Fig. 5B). The TIRFM signal (TIR) that at any point (x_0, y_0) is thus given by:

$$\begin{aligned}
&\text{TIR}(x_0, y_0) \\
&= \frac{1}{V_{TIR}} \iiint dx\,dy\,dz [FluoCa](x, y, z) \\
&\quad \times \exp\left(-\frac{(x - x_0)^2}{\sigma_x} - \frac{(y - y_0)^2}{\sigma_y}\right) \exp\left(-\frac{z}{\gamma_z}\right)
\end{aligned} \tag{11}$$

with $\sigma_x = \sigma_y = 0.0225$ μm^2 and $\gamma_z = 0.15$ μm^2 chosen to replicate the experimentally observed lateral FWHM of 250 nm and an e-fold decline over 150 nm in the axial direction. V_{TIR} is again defined as the weighted volume at the origin point:

$$V_{TIR} = \iiint dx\,dy\,dz \exp\left(-\frac{x^2}{\sigma_x} - \frac{y^2}{\sigma_y}\right) \exp\left(-\frac{z}{\gamma_z}\right) \tag{12}$$

The resting concentration of [FluoCa] is given as $[Fluo]_T/(1 + \kappa_F/[Ca^{2+}]_{Rest})$ and the average number of resting [FluoCa] molecules in volume V can then be estimated as:

$$N_{Rest}(V) = \rho_A \frac{[Fluo]_T V}{1 + \kappa_F/[Ca^{2+}]_{Rest}} \tag{13}$$

where $\rho_A = 602.2$ μM^{-1} fl^{-1}, Avogadro's number.

Ca^{2+} ions entering the cytosol space through an open channel result in a gradient of [FluoCa] around the channel pore, with an average concentration for different volumes V centered on the pore given by

$$\text{Ave}_{[FluoCa]}(V) = \frac{1}{V} \int_{-l}^{l} dx \int_{-l}^{l} dy \int_{0}^{l} dz\, [FluoCa](x, y, z) \tag{14}$$

with the rectangular volumes defined as:

$$V = \int_{-l}^{l} dx \int_{-l}^{l} dy \int_{0}^{l} dz = 4l^3 \qquad (15)$$

Then the total number of FluoCa molecules in volume V becomes:

$$N(V) = \rho_A \, \mathrm{Ave[FluoCa]}(V) \, V \qquad (16)$$

4.3. Molecular shot noise

Deterministic modeling gives a measure of the mean number of molecules within a given volume, but in real life the actual number fluctuates around this mean. The FluoCa signal is the change in FluoCa fluorescence: i.e. $N(V) - N_{\mathrm{Rest}}(V)$. From statistical dynamics, the standard deviation of this molecular shot noise is given by $\sqrt{N(V)}$, so that the signal-to-noise ratio (SNR) of a FluoCa signal can be defined as:

$$\mathrm{SNR} = \frac{N(V) - N_{\mathrm{Rest}}(V)}{\sqrt{N(V)}} \qquad (17)$$

To include the presence of molecular shot noise in simulations of SCCaFTs (Fig. 12), we generated Gaussian white noise with a standard deviation equal to the instantaneous value of $N(V)$, filtered it with a time constant of 2.3 ms matching the rate constant of initial decline of the SCCaFTs, and added it to the result of the deterministic simulation.

4.4. Photon shot noise

The Fluo signal is measured in terms of the number of emitted fluorescence photons that are detected during a given sampling interval. Statistical fluctuations in the number of photons that are detected from each FluoCa molecule thus introduce a further noise source. To simulate the presence of both molecular and photon shot noise (Fig. 3D), we first generated a series of random numbers having a binominal distribution with mean N and standard deviation $\sqrt{N}$, representing the numbers of FluoCa molecules within the measuring volume during any given sampling interval. For each individual FluoCa molecule we then generated a random number representing the number of detected photons arising from that molecule, using a Poisson distribution with mean f. The sum of detected photons arising from all the FluoCa molecules thus represents the fluorescence signal during each sampling interval.

4.5. Selection of parameters

Table 1 lists 'standard' parameter values used for simulations. These were selected as representative of experimental conditions used to image SCCaFTs arising through N-type Ca^{2+} channels expressed in *Xenopus* oocytes [13,14]. The effects of variations in individual parameters were tested in the simulations of Figs. 7–11. Unless otherwise indicated,

the other parameters in these simulations remained as given in Table 1.

4.6. A note on SI prefixes

Our simulations concern low concentrations of substances in exceedingly small volumes. We thus deal with quantities much smaller than commonly encountered in biology, and employ SI prefixes that may be unfamiliar. For convenience, these are listed below:

Factor	Name	Symbol
10^{-15}	femto	f
10^{-18}	atto	a
10^{-21}	zepto	z
10^{-24}	yocto	y

For example, a concentration of $2\,\mu M$ in a volume of $1\,\mathrm{al} = 2\,\mathrm{ymol}$ (2×10^{-24} mol; equivalent to a mean of roughly 1 atom or molecule).

5. Simulating microdomains of free Ca^{2+} and FluoCa around an open channel

5.1. Spatio-temporal distribution of free and Ca^{2+}-bound indicator around a channel

Fig. 1 shows results simulating the time courses and spatial distributions of cytosolic free Ca^{2+} and Ca^{2+}-bound indicator (FluoCa) that would result from a 10 ms duration opening of a channel that passed a Ca^{2+} current of 0.1 pA. The data were obtained using 'standard' parameters (Table 1). Families of curves in the kinetic plots (Fig. 1B and D) represent respective measurements of $[Ca^{2+}]_{\mathrm{free}}$ and [FluoCa] obtained immediately next to the channel (within 1 grid element; 50 nm × 50 nm × 50 nm), and at grid elements at increasing distances from the channel. Spatial plots (Fig. 1C and E) show corresponding radial profiles of concentration away from the channel at the end of the channel opening and at different times after it closed.

An immediate observation is that changes in free $[Ca^{2+}]$ are very large adjacent to the channel mouth ($>15\,\mu M$), and rapidly track the channel opening and closing (half-times of rise and fall both faster than 0.1 ms, Fig. 1A). Moreover, the microdomain of free Ca^{2+} (SCCaT) is highly localized (full-width at half-maximal amplitude, FWHM <80 nm at the end of the opening) and collapses within a few milliseconds of the channel closing without spreading beyond about 200 nm (Fig. 1C). In marked contrast, the corresponding profiles of [FluoCa] are appreciably blurred in time and space (Fig. 1D and E). At the end of the opening the spatial spread (FWHM = 270 nm) is about >3 times greater than

that of the free Ca^{2+} gradient that drives it and, even at the central grid element, the kinetics of Ca^{2+}-bound indicator are much slower, with half-rise and half-fall times of about 0.9 ms. As expected, these kinetics become even slower at increasing distances from the channel. These results confirm the intuitive expectation that Ca^{2+}-dependent signals with the largest dynamic range (greatest change in Ca^{2+}-bound indicator concentration) and fastest kinetics are obtained by restricting fluorescence measurements to a small volume immediately around the channel mouth. In practice, of course, the sampling volume is necessarily constrained, both by optical diffraction and the need to sample an adequate number of indicator molecules.

5.2. Effect of sampling volume on signal kinetics

We thus explored the effects of sampling the Ca^{2+}-dependent fluorescence from cytosolic volumes of various sizes, centered around the mouth of a channel that opened for 10 ms. Because indicator dyes such as Fluo-4 are almost non-fluorescent in the absence of Ca^{2+}, we consider the mean [FluoCa] throughout the volume as a linear measure of fluorescence.

Fig. 2A and B illustrate the changes in magnitude and kinetics of [FluoCa] resulting from progressive increases in sampling volume from a single model grid element (volume of 125 zl; 1.25×10^{-19} l) to the entire model volume (33.6 fl; equivalent to the sum of wide-field fluorescence from an entire cell). Smaller volumes gave signals that were both larger and faster. As a way to characterize the kinetic resolution, we measured the rate constant of the initial decline of signal following channel closure. Although the signal decay is complex and follows multiple exponential components, the initial component is well described by a single-exponential and corresponds roughly to the half-maximum threshold criterion commonly used to define channel openings in electrophysiological records. Fig. 2C shows the dependence of the initial decay rate constant on sampling volume. The temporal resolution degraded only modestly with increases in volume up to about 0.1 fl, but then showed a more abrupt decline at greater volumes.

5.3. Molecular shot noise

Deterministic (noise-free) simulations such as those in Fig. 2 make it clear that smaller sampling volumes have advantages of increasing both the kinetic resolution and the magnitude of the FluoCa concentration change. However, smaller volumes obviously encompass a smaller total *amount* of FluoCa, so that stochastic fluctuations in the number of FluoCa molecules will introduce a greater proportion of noise. Fig. 3A plots the fluorescence signal resulting from a 10 ms channel opening in terms of the increase in number of FluoCa molecules sensed within different rectangular measuring volumes (Eq. (16)). For a total Fluo concentra-
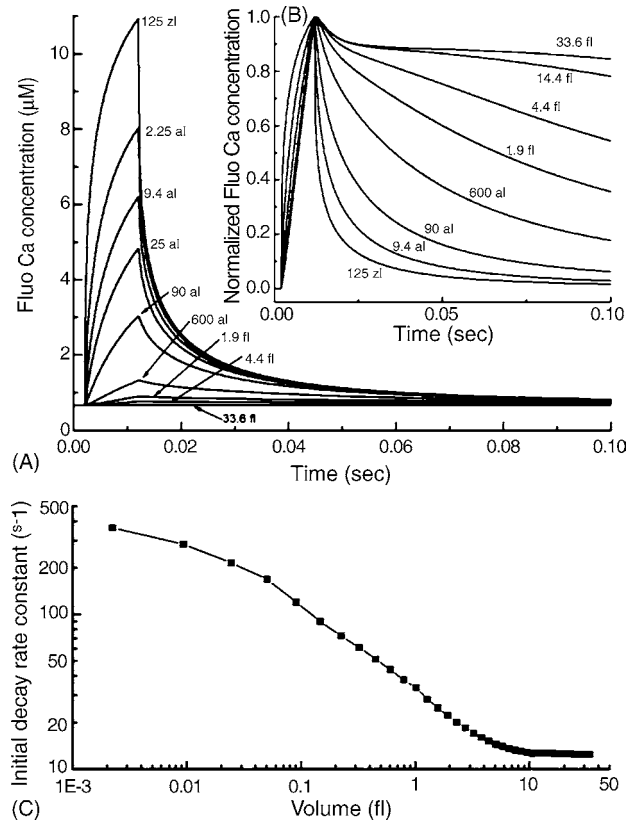

Fig. 2. Fluorescence signals (expressed as mean FluoCa concentration) as recorded from volumes of increasing size around a channel that opens for 10 ms with a Ca^{2+} current of 0.1 pA. (A) Measurements of [FluoCa] averaged throughout half-cubic regions (i.e. $x = y = 1/2z$) of various volumes ranging from 125 zl (1.25×10^{-19} l) to 33.6 fl (3.3×10^{-14} l) centered on the channel. The latter volume encompasses the entire space of the model simulation, and is equivalent to a wide-field fluorescence recording. (B) The same data, replotted after normalizing peak amplitudes to better compare differences in kinetics. (C) Influence of sampling volume on decay kinetics of the fluorescence signal. Data were obtained from single-exponential fits to the initial decay phase (first 3 ms) of traces like those in (B).

tion of 40 µM this grows from a mean of only about four molecules within a volume of 1 al, to a maximum of about 300 with volumes >1 fl that are large enough to encompass virtually all of the signal. Corresponding numbers for a total Fluo concentration of 500 µM are 20–1500 molecules.

Owing to stochastic fluctuations, the instantaneous number of molecules within a given volume will be distributed around these mean values, following a binominal distribution with a standard deviation equal to the square-root of the mean. The magnitude of this 'molecular shot noise' (i.e. $\sqrt{N(V)}$ in Eq. (17)) is plotted in Fig. 3B as a function of the sampling volume. Note that, unlike the mean signal ($N(V) - N_{Rest}(V)$), which reaches a plateau at larger volumes, the noise continues to increase. This is because the resting free $[Ca^{2+}]$ (50 nM) results in a resting level of [FluoCa], so that larger volumes encompass increasing numbers of 'basal' FluoCa molecules that contribute noise without adding any signal. The signal-to-noise ratio (SNR) predicted by Eq. (17) thus shows a biphasic dependence on sampling volume (Fig. 3C).
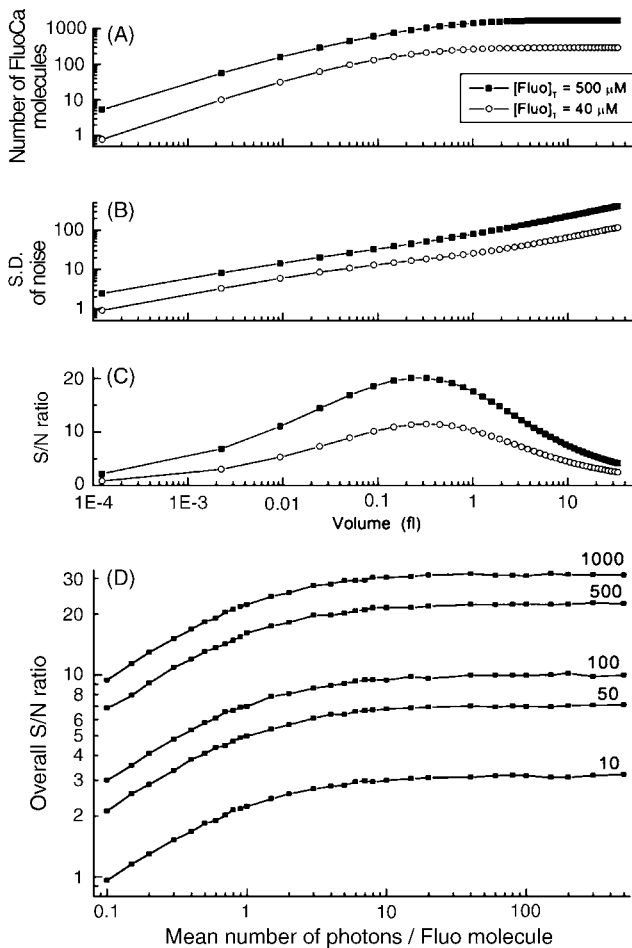
Fig. 3. Signal-to-noise ratio as functions of sampling volume and number of photons detected per Fluo molecule. (A–C) Effect of molecular shot noise on signal-to-noise ratio. Data are shown for indicator concentrations ($[Fluo]_T$) of 40 μM (open symbols) and 500 μM (filled symbols). (A) Plot shows the increase in mean number of FluoCa molecules resulting from a channel opening (0.1 pA Ca^{2+} current for 10 ms) when sampled through increasing volumes around the channel. (B) Corresponding change in signal noise with different sampling volumes, calculated as the square-root of the mean number of molecules. Note that this calculation includes 'basal' FluoCa molecules at the resting free cytosolic $[Ca^{2+}]$, in addition to those resulting from Ca^{2+} influx through the channel. (C) Signal-to-noise ratio as set by molecular shot noise, calculated by dividing data in (A) by those in (B). (D) Signal-to-noise ratio including the effects of both molecular and photon shot noise. Curves show the overall signal-to-noise ratio for various numbers of Fluo molecules in the sampling volume (indicated at right) as a function of the mean number (f) of detected photons per molecule per sampling interval. Data were generated as described in Section 4.4.

Progressive increases in volume at first give an improved signal-to-noise ratio as greater numbers of 'signal' FluoCa molecules are sampled, but ratio then degrades because the signal approaches a maximum while the noise contributed by 'basal' FluoCa molecules continues to grow. For the parameters used here, an optimal signal-to-noise ratio is achieved with a sampling volume of 0.3 fl for both low (40 μM) and high (500 μM) concentrations of total Fluo, but the ratio is better (about 20) with the high concentration than with the low concentration (about 12).

Selection of an appropriate sampling volume for optical single-channel recording thus involves a compromise. The minimum degradation of the signal-to-noise ratio is obtained with a volume around 0.3 fl (and there is no advantage in considering larger volumes), but smaller volumes provide better kinetic resolution.

5.4. Photon shot noise

Although noise arising from statistical variation in numbers of Fluo molecules in the measuring volume sets a fundamental limit to the attainable signal-to-noise ratio of SC-CaFTs, statistical variation in the number of detected photons arising from each FluoCa molecule introduces a further multiplicative source of noise. To explore how this photon shot noise affects the overall signal-to-noise ratio, we derived a family of curves (Fig. 3D) showing the effects of varying the fluorescence factor (f: the mean number of detected photons per FluoCa molecule per sampling period) for different mean numbers (N_{mean}) of FluoCa molecules. These simulations indicate that the mean amplitude of the fluorescence signal is $N_{mean}f$, and its standard deviation approaches $\sqrt{N}f$ for $f \gg 1$ and $\sqrt{Nf}$ for $f \ll 1$. Thus, the overall signal-to-noise ratio is $\sqrt{N}$ for $f \gg 1$, being limited solely by molecular shot noise; but varies as $\sqrt{Nf}$ for $f \ll 1$.

In practical terms, the noise level in fluorescence recordings of SCCaFTs will be determined almost entirely by molecular shot noise as long as the fluorescence emission can be made strong enough to produce a mean of three or more detected photons per FluoCa molecule. On the other hand, photon shot noise becomes appreciable at lower values of f, and the signal-to-noise ratio degrades to about one-half of the molecular shot noise limit for $f = 0.3$.

5.5. Signal mass revisited

We concentrate on imaging single-channel Ca^{2+} signals from very small volumes around the channel. However, a very different experimental approach involves summing the total fluorescence throughout a large surrounding volume [1,7,9]. This signal mass has generally been assumed to be proportional to a time integral of Ca^{2+} flux through the channel, provided that Ca^{2+} sequestration and extrusion mechanisms are slow on the time scale under consideration [1,9,11,18,19]. However, simulation results in Fig. 4 indicate that this assumption is not quite correct, owing to non-instantaneous equilibration of Ca^{2+} between buffers.

The sum of *total* Ca^{2+} throughout the model volume follows the expected integral of Ca^{2+} flux: that is to say, it increases linearly while the channel passes a constant current, and then remains at a fixed plateau level after the channel closes (Fig. 4A). However, while the summed concentration of FluoCa follows approximately the same pattern, it shows a small dip after the channel closes (Fig. 4C). This results from re-equilibration of Ca^{2+} between the indicator and the immobile cellular buffer (Fig. 4B), and is more marked with higher
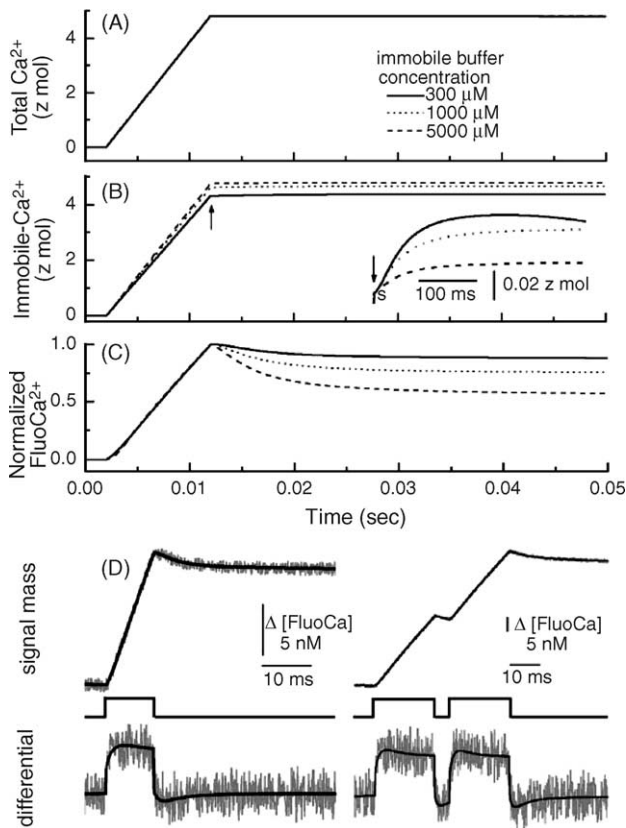
Fig. 4. Summation of Ca^{2+} signals throughout the model volume to obtain signal mass. (A–C) Signal mass is not an exact measure of integrated Ca^{2+} flux through a channel. Simulations show the kinetics of total Ca^{2+}, Ca^{2+}-bound to immobile buffer, and $FluoCa^{2+}$, summed throughout the entire model volume (33.6 fl) in response to a single-channel opening of 0.1 pA for 10 ms. (A) Total Ca^{2+} is an integral of Ca^{2+} flux. (B) Redistribution of Ca^{2+}-bound to immobile buffer after channel closure, plotted for immobile buffer concentrations of 0.3, 1 and 5 mM (marked, respectively, by solid, dotted and dashed curves). Inset shows an expanded view of the main traces, after vertical alignment at the time of channel closure (marked by arrow). (C) Corresponding kinetics of volume-averaged [FluoCa] (signal mass). Traces for different immobile buffer concentrations are normalized to the same peak amplitude. (D) Derivation of channel kinetics by differentiation of signal mass. *Upper panels* show changes in signal mass (expressed as increase in [FluoCa]) in response to a single 10 ms channel opening of 0.1 pA (left) and to two openings of 20 ms separated by a 5 ms closing (right). Smooth black lines are deterministic simulations, superimposed grey traces are after addition of Gaussian noise equal to 10% of the peak signal with the 10 ms opening. *Lower panels* show the results of differentiating the above traces. Vertical scale is arbitrary.

immobile buffer concentrations (dashed traces, Fig. 4B and C). Calibration of signal mass in terms of absolute Ca^{2+} currents may thus require additional care in cells that have high endogenous buffering capacity.

Because the signal mass approximates an integral of Ca^{2+} flux, it should be possible to recreate the flux kinetics by differentiating the signal mass. Indeed, this approach works well for noiseless records of signal mass, as illustrated by the smooth black traces in Fig. 4D, showing reconstruction of a single 10 ms opening and two 20 ms openings separated by

a 5 ms closing. The channel openings and closings are well resolved (better, in fact, than with local fluorescence measurements like those in Fig. 2A), although with some overshoot and undershoot as a result of the Ca^{2+} re-equilibration described above. A major problem, however, is that differentiation greatly accentuates any noise in the original record. The practical utility of this approach remains to be determined but, as illustrated by the grey traces in Fig. 4D, satisfactory results were still obtained after adding an arbitrary level of noise (10% of the peak signal resulting from the 10 ms channel opening) to the signal mass traces.

6. Simulation of SCCaFTs as imaged by confocal and TIRF microscopy

Several optical techniques exist that are capable of monitoring fluorescence with high time resolution from sub-femtolitre volumes. Among these, single-channel Ca^{2+} signals have been experimentally recorded using confocal microscopy [10,13,24] and TIRF microscopy [14]. We thus simulated the fluorescence signals that would be obtained with these techniques by monitoring the FluoCa concentration around a channel as weighted by the p.s.f. of the microscope (i.e. Eqs. (9) and (11)), rather than throughout an arbitrary rectangular volume as in Fig. 2.

Representative p.s.f.'s of confocal and TIRF microscopes are illustrated in Fig. 5A and B. With high-aperture objective lenses, as typically used for single-channel imaging, the confocal spot has a full width at half-maximum amplitude (FWHM) of about 0.3 μm in the lateral plane and 0.8 μm in the axial dimension (Fig. 5A) [13]. For the present simulations we assumed that the microscope was focused in the plane of the membrane, so the resulting confocal spot would appear as one half of the 'football' shape (Fig. 5A). TIRF microscopy provides a slightly better (ca. 0.25 μm FWHM) lateral resolution [14], but the major improvement over confocal microscopy lies in its enhanced axial resolution. The evanescent field formed by total-internal reflection declines exponentially with distance, so that fluorescence signals are weighted exponentially along the *z*-axis with a space constant of about 0.1 μm (Fig. 5B) [25].

Fig. 5C shows kinetic profiles of fluorescence signals resulting from a 10 ms channel opening as they would be detected by confocal and TIRF microscopy, together with measurements from a central 50 nm × 50 nm × 50 nm grid element (grey traces). The decay of fluorescence signal following channel closure is appreciably slower with both microscope modalities than the 'ideal' signal at the channel grid, but TIRFM offers somewhat better kinetic resolution than confocal microscopy (ca. 3.5 ms versus 6 ms half-decay time). In terms of spatial (lateral) resolution of SCCaFTs there is relatively little difference between confocal and TIRF microscopy, and the p.s.f.'s of both give a fluorescence signal that is appreciably broader than the underlying distribution of FluoCa (Fig. 5D).

7. Factors determining the resolution of SCCaFTs imaged by TIRFM

In the following sections we concentrate on the characteristics of TIRFM, as we believe that this methodology has practical [2,14], as well as theoretical (Fig. 5) advantages over confocal microscopy for imaging single plasma membrane channel Ca^{2+} channels. We thus simulate the fluorescence
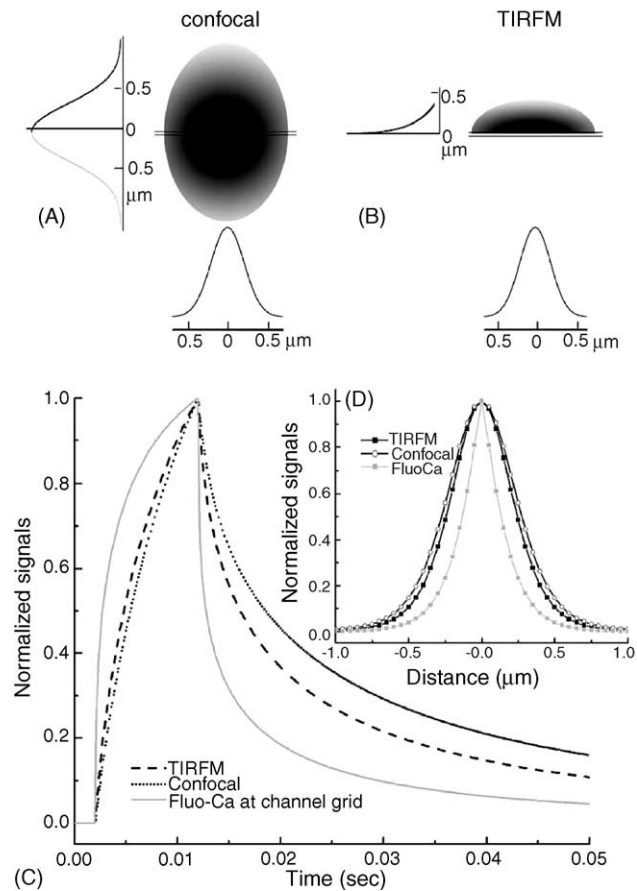

Fig. 5. Simulation of SCCaFTs imaged by confocal and TIRF microscopy. (A and B) Diagrams illustrating the three-dimensional point-spread functions of confocal and TIRF microscopes that were used to derive weighted averages of [FluoCa] in the model simulations. (A) The p.s.f. of a confocal microscope utilizing an oil-immersion objective (NA = 1.35) is distributed as Gaussian functions with widths (FWHM) of about 300 nm laterally (x and y dimensions) and 800 nm in the axial (z) dimension. For simulating cytosolic Ca^{2+} signals delineated by the plasma membrane we assumed an axial p.s.f. corresponding to the upper half of the Gaussian function. (B) The p.s.f. of a TIRF microscope with an objective lens of NA = 1.45. The lateral p.s.f. is described by a Gaussian of width (FWHM) 250 nm. The axial sensitivity declines exponentially, with a space constant of about 100 nm. (C) Simulation of SCCaFT kinetics recorded using confocal (dotted trace) and TIRFM (dashed trace) imaging modes. Model parameters are the same as in Fig. 2B and a record representing [FluoCa] at the channel grid element (grey trace) is replotted from that figure for comparison. Data are normalized to the same peak height. (D) Lateral spread of [FluoCa] at the end of a 10 ms channel opening (grey trace), and corresponding distributions of normalized Ca^{2+}-dependent fluorescence as imaged after blurring by p.s.f.'s corresponding to confocal (open symbols) and TIRF microscopes (filled symbols).

signals that would be obtained by TIRFM by computing the weighted mean [FluoCa] throughout the p.s.f. of the microscope.

7.1. Depletion of extracellular Ca^{2+}

Before investigating the intracellular Ca^{2+} signals resulting from channel opening, we first addressed a potential practical problem associated with TIRFM imaging: namely, that the plasma membrane of the cell must be closely apposed to the microscope coverglass, and thus restricts the extracellular fluid to a thin sheet sandwiched between the membrane and glass. Ca^{2+} influx through channels might thus result in local depletion of extracellular Ca^{2+}, thereby reducing the single-channel Ca^{2+} current itself. To estimate the extent of this depletion, we simulated the profile of extracellular $[Ca^{2+}]$ around the mouth of an open channel carrying a current of 0.1 pA for 100 ms, assuming free diffusion ($D = 200\ \mu m^2\ s^{-1}$) within a film of extracellular fluid ($40\ \mu m \times 40\ \mu m \times 50\ nm$ deep) containing 6 mM Ca^{2+}. As shown in Fig. 6, depletion of extracellular Ca^{2+} is restricted to <1 μm around an open channel and, most significantly, re-
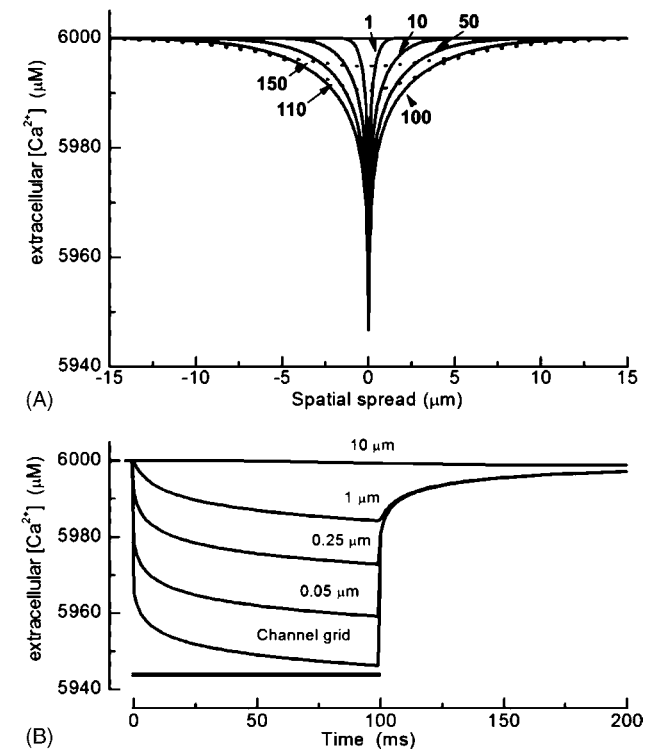

Fig. 6. Depletion of Ca^{2+} in the thin extracellular fluid film is minimal during TIRFM imaging of single-channel events. (A) Spatial profiles of $[Ca^{2+}]$ in a 50 nm thick film of extracellular fluid around the mouth of a channel passing a Ca^{2+} current of 0.1 pA. Solid curves of increasing width show profiles 1, 10, 50 and 100 ms following opening of the channel. Dotted curves show profiles 10 and 50 ms after the channel closed. (B) Temporal profiles showing changes in extracellular $[Ca^{2+}]$ during a 100 ms channel opening (marked by bar), measured in 50 nm square grid elements centered on the channel mouth and at the indicated distances away from the channel.
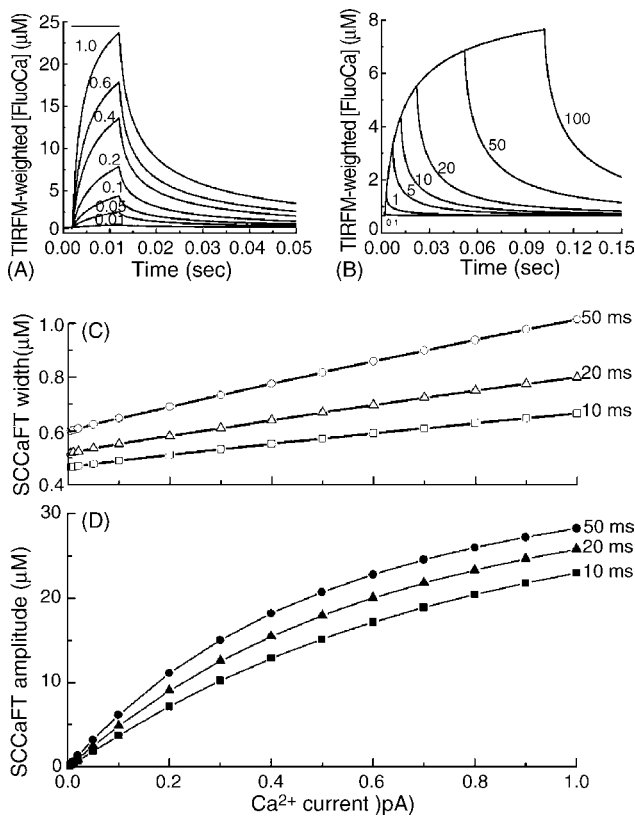
Fig. 7. Simulation of TIRFM SCCaFTs for different single-channel Ca²⁺ currents and channel open durations. Simulations were performed using the 'standard' model parameters and TIRFM imaging parameters listed in Table 1. (A) Simulated TIRFM signals in response to 10 ms channel openings with single-channel currents ranging between 0.005 and 1 pA, as indicated. Data are expressed as a weighted average of the [FluoCa] increase throughout the TIRFM sampling volume; a measure that corresponds linearly to experimentally observed fluorescence. (B) SCCaFT kinetics for different durations of channel openings (indicated in ms), with a constant Ca²⁺ current of 0.1 pA. (C and D) Spatial width and peak amplitude of SCCaFTs as a function of single-channel Ca²⁺ current, plotted for channel open durations of 10 ms (squares), 20 ms (triangles) and 50 ms (circles).

sults in a negligible (ca. 1%) drop in [Ca²⁺] from 6 to 5.95 mM even in the immediate vicinity of the channel. In the following simulations we thus assume that extracellular [Ca²⁺] remains constant at 6 mM.

7.2. TIRFM SCCaFTs as a function of single-channel current and open duration

Ideally, fluorescence signals should provide a measure that is linearly proportional to single-channel Ca²⁺ current over a wide range of currents and channel open durations. Fig. 7 shows the results of simulations to explore these relationships. SCCaFTs (i.e. [FluoCa] weighted by the TIRFM p.s.f.) resulting from single-channel currents varying between 0.01 and 1 pA with constant (10 ms) duration are shown in Fig. 7A, whereas Fig. 7B illustrates simulations where the current was fixed at 0.1 pA while the channel opening duration was varied between 0.1 and 100 ms.

Selected measurements from such simulations show the dependence of the spatial width (Fig. 7C) and peak amplitude (Fig. 7D) of SCCaFTs on single-channel current for open durations of 10, 20 and 50 ms. The amplitude of the fluorescence signal increases progressively with single-channel current for all durations, but a reasonably linear relationship holds only for currents up to about 0.2 pA. Moreover, the peak fluorescence amplitude is strongly affected by the channel open duration, such that a 10 ms opening results in a signal little more than one-half of the steady-state value (Fig. 7B). The spatial width (FWHM) of SCCaFTs increases with both increasing current and open duration, but the dependence is quite shallow and the FWHM changes only within a range of about 0.5–1.0 μm from very small, brief channel openings to a current of 1 pA for 50 ms.

7.3. Effects of indicator concentration

Results presented above (Fig. 3) indicate that the available number of FluoCa molecules in the imaging volume is a major factor determining the signal-to-noise ratio with which SCCaFTs can be recorded. Moreover, the kinetics of the fluorescence signal depend strongly on the binding of Ca²⁺ to Fluo, and the subsequent diffusion of FluoCa from the measuring volume. We thus investigate the effects of systematically changing the cytosolic concentration of indicator dye.

SCCaFTs evoked by a 0.1 pA, 10 ms channel opening are simulated in Fig. 8A for Fluo concentrations ([Fluo])ₜ between 1 μM and 10 mM, and the inset shows the same data after normalizing to the same peak amplitude to facilitate comparison of kinetics. Higher total concentrations of Fluo result in larger signals, and speed the kinetics of SCCaFTs so that the fluorescence more closely tracks the channel opening and closing. The speeding arises because most Ca²⁺ ions entering through the channel bind rapidly to Fluo molecules, rather than to immobile buffer, and free diffusion of FluoCa results in a rapid decay of local fluorescence after the channel closes. Conversely, most Ca²⁺ ions will bind to immobile buffer at low indicator concentrations, resulting in slowed fluorescence kinetics because diffusion of Ca²⁺ is hampered by repeated rebinding to the stationary buffer.

The signal amplitude increases non-linearly with [Fluo]ₜ (filled symbols, Fig. 8B), and approaches a maximum at concentrations above about 1 mM where the availability of Ca²⁺ ions becomes limiting. Different from this, the signal-to-noise ratio reaches a maximum at a Fluo concentration of about 500 μM, and actually degrades at higher concentrations (open symbols, Fig. 8B). The reason for this is that there is little further gain in 'signal' FluoCa molecules because most of the Ca²⁺ ions entering through the channel are already bound, whereas increasing concentrations of Fluo continue to bind increasing numbers of 'basal' Ca²⁺ ions at the resting free concentration of 50 nM, and thus contribute additional noise variance. Finally, Fig. 8C plots the decay rate of SCCaFTs following channel closure as a function of
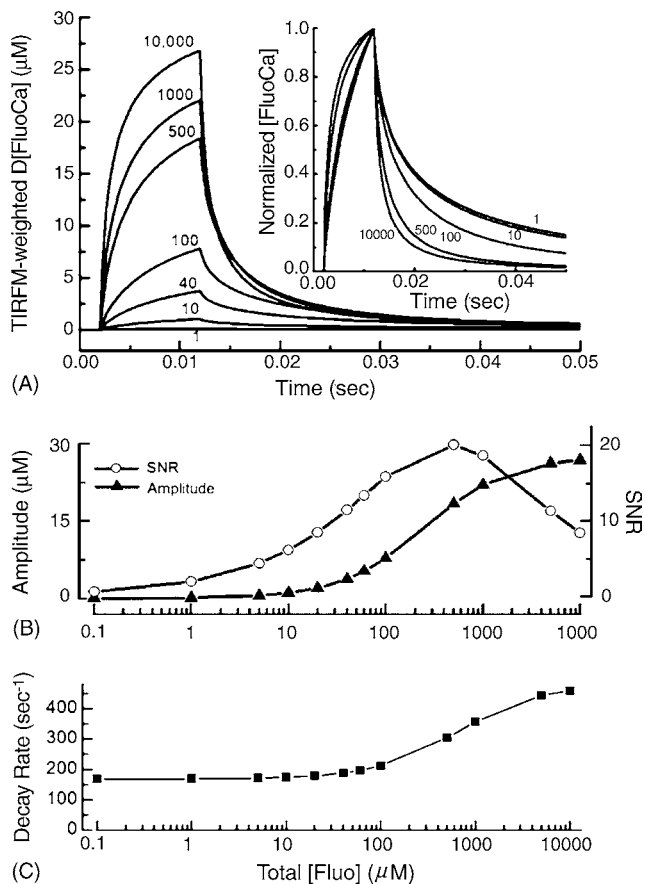
Fig. 8. Dependence of fluorescence signals on intracellular concentration of indicator dye. (A) Traces show TIRFM-weighted [FluoCa] signals in response to a single-channel current of 0.1 pA for 10 ms with Fluo concentrations varying between 1 and 1000 μM, as indicated. The inset shows the same data after normalizing peak amplitudes so as to facilitate comparison of rise and decay kinetics. (B) Peak amplitude (filled triangles) and signal-to-noise ratio (open circles) of signals evoked by a 0.1 pA, 10 ms channel current as functions of intracellular [Fluo]$_T$. Data were obtained by simulations employing a measuring volume of 0.3 fl, chosen to provide optimal signal-to-noise ratio. (C) Corresponding initial decay rate of SCCaFTs as a function of [Fluo]$_T$.

[Fluo]$_T$. This remains essentially constant for concentrations up to about 100 μM, but then increases nearly three-fold with concentrations up to 10 mM as the concentration of indicator becomes appreciable in comparison to the concentration of immobile buffer sites.

These simulations were performed using parameters for the Fluo indicator matching those of Fluo-4 dextran. With this dye it appears that an intracellular concentration of 400–1000 μM is likely to provide an optimum compromise between signal-to-noise ratio and kinetic resolution.

7.4. Influence of indicator diffusion coefficient

Many Ca^{2+} indicator dyes are available as free salts, and as various dextran conjugates. Given that the diffusion coefficient of a molecule slows roughly in proportion to the cube root of its molecular weight it is, therefore, possible to chose
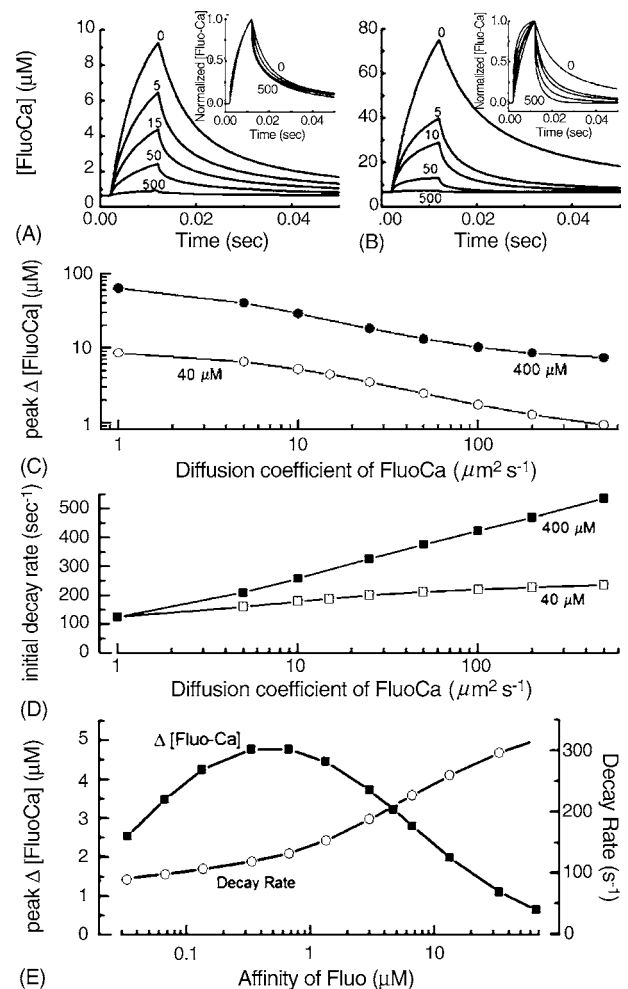

Fig. 9. Effects of varying the diffusion coefficient and affinity of the indicator dye. (A) Simulated SCCaFTs generated by a single-channel current of 0.1 pA for 10 ms, imaged using indicator (total concentration = 40 μM) with diffusion coefficients (D_{CaF}) varying between 0 and 500 μm^2 s^{-1}, as indicated. Inset shows the same traces, after normalizing to the same peak amplitudes. (B) Equivalent results obtained with an intracellular indicator concentration of 400 μM. (C) Peak amplitude of SCCaFTs (single-channel current of 0.1 pA for 10 ms) as a function of D_{CaF} for Fluo concentrations of 40 μM (open circles) and 400 mM (filled circles). (D) Initial decay rate of SCCaFTs accelerates with increasing D_{CaF}. Data show Fluo concentrations of 40 μM (open squares) and 400 μM (filled squares). (E) Dependence of SCCaFT amplitude (filled squares) and initial decay rate (open circles) on affinity of the indicator. The affinity was changed by altering the rate of Ca dissociation (β_F) while maintaining the binding rate (α_F) fixed at 150 μM^{-1} s^{-1}. D_{CaF} was 15 μm^2 s^{-1}.

among indicators whose diffusion coefficient varies over a certain range.

Simulations of SCCaFTs imaged using indicator of varying diffusion coefficients, but otherwise identical properties, are shown in Fig. 9A and B for respective total indicator concentrations of 40 and 400 μM. With both concentrations the signal amplitude declines progressively with increasing diffusion coefficient (Fig. 9C), because FluoCa molecules with higher motility can diffuse more rapidly out of the measuring volume. In terms of SCCaFT kinetics, changes in Fluo dif-

fusion coefficient over a wide range have little effect when using a low (40 μM) indicator concentration, whereas the decay rate is appreciably speeded with increasing diffusion coefficient for the high (400 μM) concentration (Fig. 9D). The explanation for this is that only a small proportion of Ca^{2+} ions entering through the channel will be captured by Fluo if the indicator concentration is low, so that clearance of Ca^{2+} from the measuring volume following channel closure is largely determined by the diffusion of free Ca^{2+}; whereas, as noted previously, diffusion of FluoCa predominates at higher indicator concentrations.

7.5. Indicator affinity

Fluorescent indicators are available with Ca^{2+} dissociation constants varying across a wide range from a few hundred nM to tens of μM [26]. We thus performed simulations to determine the optimal value for imaging SCCaFTs. As illustrated in Fig. 9E (filled symbols), the largest fluorescence signals were obtained with a dissociation constant around 1 μM. Lower affinities (i.e. larger dissociation constants) resulted in smaller signals because the dye bound less Ca^{2+}, whereas higher affinities resulted in an increasing proportion of the indicator being bound by Ca^{2+} in the resting state, leaving fewer dye molecules to respond to Ca^{2+} ions entering through the channel. Moreover, the SCCaFT decay kinetics slowed as the dissociation constant of the indicator was increased (Fig. 9E, open symbols), such that an optimal compromise between signal amplitude and kinetics probably lies with dissociation constants between 1 and 5 μM.

The dissociation constant κ is given by the ratio of the rate constant for Ca^{2+} unbinding (β) divided by the rate for Ca^{2+} binding (α). Although published values are available for the dissociation constants of different indicators [26], this is only rarely the case for the rate constants [27]. For the simulations in Fig. 9E we set the affinity by varying β while keeping α fixed at 150 μM^{-1} s^{-1}. In other simulations (not shown) we maintained a fixed dissociation constant (3 μM) while altering both α and β in parallel. In that case, SCCaFT amplitudes increased and their kinetics accelerated progressively with increases in α from about 10 to 1000 μM^{-1} s^{-1}, indicating that more rapidly equilibrating indicators are preferable in terms of both signal-to-noise ratio and kinetics.

7.6. Addition of mobile cytosolic Ca^{2+} buffers

For simplicity, the above simulations did not consider any mobile cytosolic Ca^{2+} buffer other than the indicator dye itself. To study the effects of endogenous mobile Ca^{2+}-binding proteins that might be present in a cell, and to explore the effects of adding exogenous buffer, we simulated SCCaFTs in the presence of increasing concentrations of freely mobile buffers with differing binding kinetics.

As expected, the addition of a buffer with rapid Ca^{2+} binding kinetics like BAPTA (Table 1) progressively reduces the amplitude of the fluorescence signals (Fig. 10A and B), be-
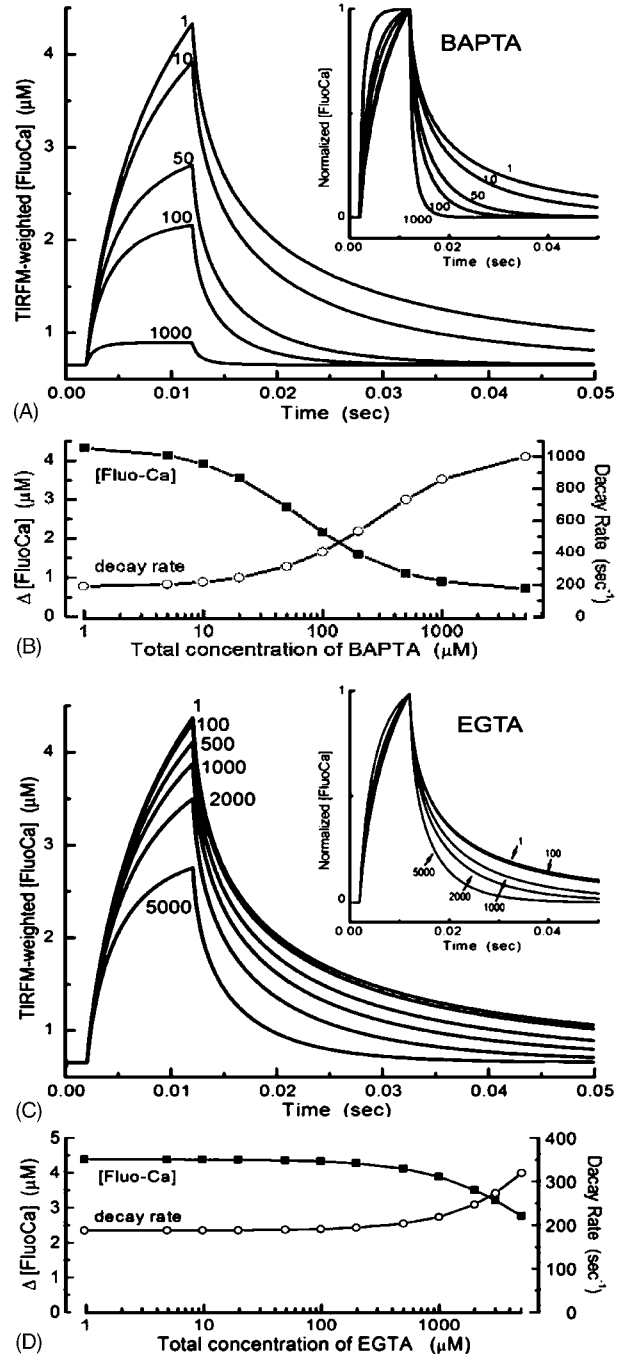

Fig. 10. Actions of exogenous mobile buffers with differing binding kinetics. (A) Traces show simulated TIRFM-weighted [FluoCa] signals in response to a single-channel current of 0.1 pA for 10 ms in the presence of different intracellular concentrations (indicated in μM) of the fast mobile buffer BAPTA. The inset shows the same data after normalizing peak amplitudes so as to facilitate comparison of rise and decay kinetics. (B) Dependence of SCCaFT amplitude (filled squares) and initial decay rate (open circles) on BAPTA concentration. (C and D) Analogous data to (A) and (B), for the slowly-binding buffer EGTA.

cause a greater proportion of the Ca^{2+} ions entering through the channel rapidly complex to BAPTA and are thus unavailable to bind to Fluo. In parallel with this reduction in signal amplitude, increasing concentrations of BAPTA accelerate

the rise and decay kinetics of SCCaFTs (Fig. 10A and B), acting as a 'shuttle' buffer with high diffusion coefficient to rapidly carry Ca^{2+} ions away from the measuring volume. Thus, cell types expressing low levels of endogenous mobile buffer will provide larger SCCaFTs and, although BAPTA-loading of a cell offers a way to improve the kinetic resolution of single-channel Ca^{2+} signals, this comes at expense of a greatly reduced signal amplitude.

We also simulated the effects of introducing a mobile buffer with slow binding kinetics like those of EGTA (Table 1). As shown in Fig. 10C and D, cytosolic concentrations up to about 1 mM produced slight changes in SCCaFT amplitude, kinetics and spatial spread. However, at a concentration of 5 mM the decay kinetics were speeded nearly two-fold, with only a modest (ca. 30%) reduction in peak amplitudes. High concentrations of EGTA may, therefore, be experimentally useful to enhance kinetic resolution, and may also help reduce the slow rise in baseline Ca^{2+}-fluorescence observed during repetitive channel openings [13,14].

7.7. Immobile Ca^{2+} buffer

Finally, we examined the results of varying the concentration of immobile buffer, which was fixed at 300 μM in all other simulations. As shown in Fig. 11A and B, increasing concentrations of immobile buffer reduced the amplitude of SCCaFTs but, in contrast to mobile buffers, slowed rather than accelerated their kinetics.

8. Discussion

The use of optical approaches to monitor single-channel activity is still in its infancy, but imaging of local fluorescence signals (SCCaFTs) generated by Ca^{2+} influx through individual, Ca^{2+}-permeable membrane channels holds great promise, and offers capabilities beyond those of existing electrophysiological methods. The ultimate limits to the resolution that can be achieved by such optical single-channel recordings are set by the diffusion and binding of Ca^{2+} ions within the cytosolic microenvironment around a channel mouth; processes that are reasonably well characterized and are thus amenable to quantitative modeling. Here we used simulations to help understand the generation of SCCaFTs, and to aid the development of improved experimental imaging methodologies.

8.1. Kinetic resolution

A major goal is to develop techniques to image fluorescence signal that track the opening and closing of individual channels with a temporal resolution approaching that of the patch-clamp. The fundamental limit arises in the kinetics of the fluorescence signal itself, since fast c.c.d. cameras and linescan or spinning-disc confocal microscopes can image at rates of several hundred per second or better. Our simulations show that the kinetics of SCCaFTs recorded from localized cytosolic volumes improve progressively with decreasing size of the sampling volume. However, this involves a compromise, because smaller volumes encompass less indicator dye (Fluo), and thus provide smaller and noisier signals. Volumes around 0.1 fl appear to offer a good compromise, and match well with the volumes of the 'focal spot' achieved using confocal or TIRF microscopy. TIRFM permits a smaller sampling volume, and hence better kinetic resolution than does confocal microscopy, but this advantage is modest (Fig. 5C), and choice between the two modalities lies more with practical matters of implementation. TIRFM cannot be used to image intracellular channels deep (>about 100 nm) within a cell, but for plasma membrane channels it has advantages of simplicity and low cost, and is restricted in temporal resolution only by the camera frame rate.

In addition to the sampling volume, the kinetic resolution is determined by several other factors, including the rate of Ca^{2+} binding to Fluo, and the diffusion of free- and bound-Ca^{2+} out of the sampling volume. Increasing the cytosolic Fluo concentration has beneficial effects of both speeding the fluorescence signals and increasing their amplitude (Fig. 8), whereas indicators with faster diffusion coefficients speed the
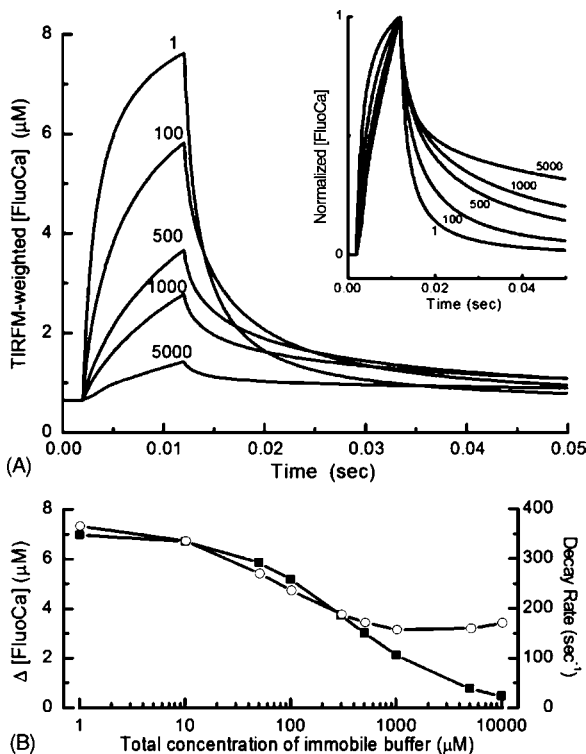

Fig. 11. Dependence of SCCaFTs on the cytosolic concentration of endogenous, immobile Ca^{2+} buffer. (A) Traces show simulated TIRFM-weighted [FluoCa] signals in response to a single-channel current of 0.1 pA for 10 ms in the presence of different intracellular concentrations of immobile buffer. The inset shows the same data after normalizing peak amplitudes so as to facilitate comparison of rise and decay kinetics. (B) Dependence of SCCaFT amplitude (filled squares) and initial decay rate (open circles) on immobile buffer concentration.

kinetics but considerably reduce signal amplitude (Fig. 9C and D). Addition of mobile exogenous buffer could also be used to speed the signal kinetics, but again at the cost of a reduced amplitude. In this regard, buffers with slow binding kinetics like EGTA appear to represent a better compromise than fast buffers such as BAPTA. Lastly, increasing amounts of endogenous immobile cellular Ca^{2+} buffers diminish the fluorescence signal and slow its kinetics, most especially by accentuating the slow 'tail' of fluorescence decay after channel closure (Fig. 10C and D). Thus, imaging of SCCaFTs will be facilitated in cell types that have relatively weak endogenous buffering power.

Our simulations indicate that, under optimal conditions, it should be possible to record SCCaFTs that track channel gating with a rate constant of roughly $500\,s^{-1}$. This is sufficient to resolve channel openings with durations of one or a few ms, but would not be adequate, for example, in the case of N-type voltage-gated channels that show mean open times <1 ms. However, the processes that filter the fluorescence signals are reproducible and well characterized so it may be possible to develop post hoc algorithms to partially correct for the high-frequency roll-off, in a manner analogous to the 'boost' circuits used to compensate the restricted frequency response of patch-clamp headstages.

8.2. Signal-to-noise considerations

Our results (Fig. 3) indicate that the major noise source in recording SCCaFTs is likely to be molecular shot noise inherent in the fluorescence signal itself. In order to achieve good kinetic resolution, fluorescence must be monitored from small cytosolic volumes (0.1 fl or less)—typically encompassing no more than a few hundred FluoCa molecules. Statistical fluctuations thus lead to noise ('molecular shot noise'), with a standard deviation equal to the square-root of the mean number of molecules present. Because the temporal characteristics of this noise are determined by the same processes that generate the signal itself (stochastic molecular binding and diffusion), it is unlikely that low-pass filtering in the frequency domain will achieve any substantial improvement without unacceptable distortion. Strategies to improve the signal-to-noise ratio, therefore, involve increasing the number of 'signal' FluoCa molecules within the sampling volume. Within a limited range this is possible by varying the sampling volume itself—for example, by integrating the fluorescence over several adjacent pixels in a TIRFM image. However, this involves a trade-off with degraded kinetic resolution and, beyond a certain point (volumes >about 0.3 fl), the signal-to-noise ratio actually begins to degrade because of noise contributed by Fluo molecules binding 'resting' Ca^{2+} ions. Instead, a good solution is simply to increase the total concentration of intracellular indicator, which results an improvement in both signal-to-noise ratio (Fig. 8B) and in kinetics (Fig. 8C). Higher Fluo concentrations will, of course, perturb physiological Ca^{2+} signals—but for the purpose of

studying channel function that may not be a disadvantage and, indeed, may have advantages such as suppressing Ca^{2+}-dependent channel inhibition.

It should be possible to minimize any further noise introduced when using fluorescence imaging to sample the number of Fluo molecules in the focal volume. Photonics technology has now advanced to the point where single photons can be detected with high efficiency (quantum efficiency 50–90%) and with virtually no dark noise or readout noise, using either intensified c.c.d. cameras or c.c.d. cameras with on-chip electron multiplication [28]. The remaining additional source of noise then arises from statistical variation in the number of photons detected. As illustrated in Fig. 3D, this photon shot noise results in appreciable degradation of the overall signal-to-noise ratio if the mean number of photons detected during a given sampling interval from each FluoCa molecule (f) is <1, but for values of $f > 3$ the ratio closely approaches the limit set by molecular shot noise. Even though the excitation intensities that can be applied to living cells are severely limited by phototoxicity and photobleaching, it appears that values of $f > 3$ can be readily achieved. For example, Zou et al. [9] report a fluorescence factor f of about 2.4 detected photons per Ca^{2+}-bound Fluo-3 molecule per 10 ms exposure time under the conditions of their cellular imaging experiments. In that case, the predominant noise source will be molecular, and not photonic. A final caveat, however, is that this situation may be achieved only with relatively long sampling intervals—such as the exposure times (typically several ms) of a c.c.d. camera used to image TIRFM signals. In a point-scanning confocal microscope, much higher (ca. 1000×) fluorescence excitation intensities would be required to achieve a comparable value of f within typical pixel dwell times only a few microseconds, risking problems of fluorophore saturation and photodamage.

Noise considerations make an interesting contrast between optical and electrophysiological means of monitoring single-channel activity. The inherent noise in a single-channel current is small (because thousands of ions typically flow per millisecond), and the major noise sources arise in the external instrumentation—primarily the patch pipette and the amplifier. Different from this, photons can be detected with little or no instrumental noise, and the major noise source arises within the cell from the signal itself.

8.3. Spatial resolution

A major advantage of single-channel imaging techniques over electro-physiological recording is that they provide spatial information, allowing individual channels to be mapped and tracked over time [7,13,14]. A very fine resolution is possible. Simulations using our 'standard' conditions show that FluoCa spreads with a FWHM of only about 250 nm during a 10 ms channel opening, so that the width of experimentally observed SCCaFTs (FWHM: ~600 nm, [13,14])

is determined substantially by the microscope p.s.f. Thus, it should be possible to separately resolve simultaneously open channels as close as about $0.5\,\mu m$, and cross-talk between fluorescence measurements from channels more than about $1\,\mu m$ apart will be minimal. Moreover, under conditions of low opening probability it is possible to define the centroid of the SCCaFT arising from an isolated channel opening with a much higher resolution, constrained only by noise considerations and not by diffusion or diffraction.

8.4. Estimation of single-channel Ca^{2+} current amplitudes

Patch-clamp records provide an unambiguous and absolute measure of the current flowing through an individual channel. In this regard, optical imaging of local fluorescence signals is considerably inferior. Firstly, it is problematic to calibrate SCCaFTs in terms of the absolute flux of Ca^{2+} ions (i.e. Ca^{2+} current) through a channel, because the fluorescence depends on several poorly-characterized parameters (including the microscope p.s.f., endogenous buffers, and properties of the indicator within a cytosolic environment), and is subject to non-linearities resulting from local saturation of Fluo and endogenous buffers. The most practicable experimental approach is to perform an empirical calibration, specific for a particular cell type and imaging configuration, by simultaneously acquiring fluorescence and patch-clamp data from a given channel [1,3,8,9,12]. Even then, the local SCCaFT amplitude varies as a linear function of Ca^{2+} current over a restricted range (currents <about 0.3 pA, Fig. 7D), and attains a steady-state value only for channel openings longer than about 50 ms (Fig. 7B). Moreover, we emphasize that the extreme narrowness of free Ca^{2+} gradients around single-channels (SCCaTs), and the marked disparity between distributions of free $[Ca^{2+}]$ and [FluoCa], make it meaningless to attempt to calibrate the fluorescence in terms of local free Ca^{2+} concentration.

An alternative approach is to measure the total fluorescence ('signal mass'), summed throughout a cellular volume sufficiently large to encompass virtually all the signal [1,9,18]. This substantially eliminates non-linearities, and gives a measure directly related to the integral of Ca^{2+} flux through a channel, although the proportionality constant must still be calibrated with reference to patch-clamp current measurements [9]. In principle, differentiation of the signal mass can be used to obtain the underlying Ca^{2+} flux; and, indeed, simulations show that this approach can give at least as good a resolution of channel kinetics (Fig. 4D) as obtained by local fluorescence measurements. Whether this is experimentally feasible remains to be determined, since differentiation greatly accentuates any noise in the original signal. Moreover, the signal mass approach is restricted to situations where only one channel is active within a large area of the cell, whereas highly-localized measurements of SCCaFTs have the potential to independently monitor channels at densities approaching $1\,\mu m^{-2}$.
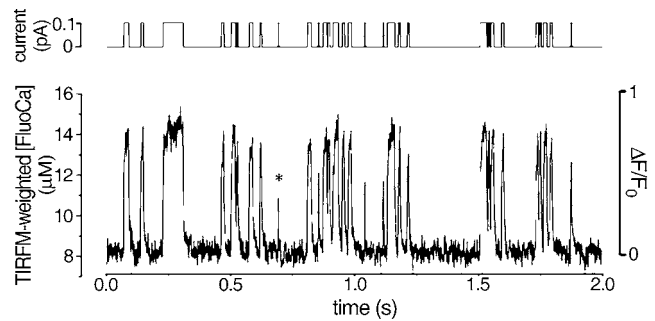

Fig. 12. Simulated SCCaFTs, including molecular shot noise, evoked by a sequence of stochastic channel openings. Parameters were chosen to provide an optimal subjective compromise between kinetic resolution and signal-to-noise ratio. Specifically: $[Fluo]_T = 500\,\mu M$; $D_{Fluo} = 50\,\mu m^2\,s^{-1}$, cytosolic $[EGTA] = 2\,mM$; sampling volume increased to 0.03 fl by summing the signal throughout a grid of 5×5 adjacent pixels at 50 nm spacings, with each pixel representing the TIRFM p.s.f. See Section 4.2 for further details. The upper trace shows representative stochastic openings of a single-channel. The lower trace shows the resulting fluorescence signals, scaled both as the average Fluo concentration within the sampling volume (left axis), and as a fluorescence ratio change ($\Delta F/F_0$: right axis) relative to the resting fluorescence with the channel closed. The shortest channel opening (marked by asterisk) had a duration of 1 ms.

8.5. Conclusion

To demonstrate the potential capabilities of optical single-channel recording, we show in Fig. 12 simulated SCCaFTs arising from a sequence of channel openings. The simulation includes noise arising from molecular fluctuations, and the imaging parameters (indicator concentration, sampling volume, addition of EGTA, etc.) were chosen to give a good subjective compromise between kinetic speed and signal-to-noise ratio. This illustration thus represents the optimal resolution that may be obtained with 'raw' fluorescence records, and further improvement may be possible by post-processing to partially correct for low-pass filtering inherent in the local Fluo signal. Published experimental records [1–3,7–14,24] do not approach this level of resolution, but there appear to be no fundamental limitations or technical hurdles that would prevent its practical attainment. We thus believe that fluorescence imaging techniques hold great promise for single-channel studies of the numerous types of ion channels that display significant Ca^{2+} permeability.

Acknowledgments

References

[1] H. Zou, L.M. Lifshitz, R.A. Tuft, K.E. Fogarty, J.J. Singer, Imaging calcium entering the cytosol through a single opening of plasma

membrane ion channels: SCCaFTs-fundamental calcium events, Cell Calcium 35 (2004) 523–533.

[2] A. Demuro, I. Parker, Optical single-channel recording: imaging Ca^{2+} flux through individual ion channels with high temporal and spatial resolution, J. Biomed. Opt., in press.

[3] S.Q. Wang, W.C. Wei, G. Zhao, D.X. Brocket, J. Shen, L.S. Song, W. Wang, D. Yang, H. Cheng, Imaging microdomain Ca^{2+} in muscle cells, Circ. Res. 94 (2004) 1011–1022.

[4] M.J. Berridge, Elementary and global aspects of calcium signaling, J. Physiol. 499 (1997) 291–306.

[5] I. Parker, Y. Yao, Ca^{2+} transients associated with openings of inositol trisphosphate-gated channels in *Xenopus* oocytes, J. Physiol. 491 (1996) 663–668.

[6] P. Lipp, E. Niggli, Submicroscopic calcium signals as fundamental events of excitation–contraction coupling in guinea-pig cardiac myocytes, J. Physiol. 492 (1996) 31–38.

[7] H. Zou, L.M. Lifshitz, R.A. Tuft, K.E. Fogarty, J.J. Singer, Imaging Ca^{2+} entering the cytoplasm through a single opening of a plasma membrane cation channel, J. Gen. Physiol. 114 (1999) 575–588.

[8] H. Zou, L.M. Lifshitz, R.A. Tuft, K.E. Fogarty, J.J. Singer, Visualization of Ca^{2+} entry through single stretch-activated cation channels, Proc. Natl. Acad. Sci. U.S.A. 99 (2002) 6404–6409.

[9] H. Zou, L.M. Lifshitz, R.A. Tuft, K.E. Fogarty, J.J. Singer, Using total fluorescence increase (signal mass) to determine the Ca^{2+} current underlying localized Ca^{2+} events, J. Gen. Physiol. 124 (2004) 259–272.

[10] S.Q. Wang, L.S. Song, E.G. Lakatta, H. Cheng, Ca^{2+} signalling between single L-type Ca^{2+} channels and ryanodine receptors in heart cells, Nature 410 (2001) 592–596.

[11] S.Q. Wang, M.D. Stern, E. Rios, H. Cheng, The quantal nature of Ca^{2+} sparks and in situ operation of the ryanodine receptor array in cardiac cells, Proc. Natl. Acad. Sci. U.S.A. 101 (2004) 3978–3984.

[12] R. ZhuGe, K.E. Fogarty, R.A. Tuft, L.M. Lifshitz, K. Sayar, J.V. Walsh Jr., Dynamics of signaling between Ca^{2+} sparks and Ca^{2+}-activated K^+ channels studied with a novel image-based method for direct intracellular measurement of ryanodine receptor Ca^{2+} current, J. Gen. Physiol. 116 (2000) 2298–2306.

[13] A. Demuro, I. Parker, Optical single-channel recording: imaging Ca^{2+} flux through individual N-type voltage-gated channels expressed in *Xenopus* oocytes, Cell Calcium 34 (2003) 499–509.

[14] A. Demuro, I. Parker, Imaging the activity and localization of single voltage-gated Ca^{2+} channels by total internal reflection microscopy, Biophys. J. 86 (2004) 3250–3259.

[15] A. Demuro, I. Parker, Optical imaging of single-channel activity of muscle nicotinic receptors, Soc. Neurosci. Abstr. (2004), program 707.7.

[16] E. Neher, B. Sakman, Single-channel currents recorded from membrane of denervated frog muscle fibres, Nature 260 (1976) 799–802.

[17] A. Sonnleitner, L.M. Mannuzzu, S. Terakawa, E.Y. Isacoff, Structural rearrangements in single ion channels detected optically in living cells, Proc. Natl. Acad. Sci. U.S.A. 99 (2002) 12759–12764.

[18] X.P. Sun, N. Callamaras, J.S. Marchant, I. Parker, A continuum of *Ins*P3-mediated elementary Ca^{2+} signaling events in *Xenopus* oocytes, J. Physiol. Lond. 509 (1998) 67–80.

[19] S. Hollingworth, J. Peet, W.K. Chandler, S.M. Baylor, Calcium sparks in intact skeletal muscle fibers of the frog, J. Gen. Physiol. 118 (2001) 653–678.

[20] M. Naraghi, E. Neher, Linearized buffered Ca^{2+} diffusion in microdomains and its implications for calculation of $[Ca^{2+}]$ at the mouth of a calcium channel, J. Neurosci. 17 (1997) 6961–6973.

[21] C.J. Mainrenken, J.G. Borst, B. Sakmann, Local routes revisited; the space and time dependence of the Ca^{2+} signal for phasic transmitter release at the rat calyx of Held, J. Physiol. 547 (2003) 665–689.

[22] W.M. Roberts, Spatial calcium buffering in saccular hair cells, Nature 363 (1993) 74–76.

[23] R. Thul, M. Falke, Release currents of IP3 receptor channel clusters and concentration profiles, Biophys. J. 86 (2004) 2660–2673.

[24] S. Peng, N.G. Publicover, G.J. Kargacin, D. Duan, J.A. Airey, J.L. Sutko, Imaging single cardiac ryanodine receptor Ca^{2+} fluxes in lipid bilayers, Biophys. J. 86 (2004) 134–144.

[25] D. Axelrod, Total internal reflection microscopy in cell biology, Methods Enzymol. 361 (2003) 1–33.

[26] R.P. Haugland, Handbook of fluorescent probes and research products, ninth edition. Molecular Probes Inc., Eugene, OR.

[27] M. Eberhard, P. Erne, Kinetics of calcium binding to fluo-3 determined by stopped-flow fluorescence, Biochem. Biophys. Res. Commun. 163 (1989) 309–314.

[28] P. Colarusso, K.R. Spring, Imaging at low light levels with cooled and intensified charge-coupled device cameras, Methods Enzymol. 360 (2003) 383–394.

[29] N.L. Allbritton, T. Meyer, L. Stryer, Range of action of calcium ion and inositol 1,4,5-trisphosphate, Science 258 (1992) 1812R–1825R.

[30] K.R. Gee, K.A. Brown, W.N.U. Chen, J. Bishop-Stewart, D. Gray, I. Johnson, Chemical and physiological characterization of fluo-4 Ca^{2+}-indicator dyes, Cell Calcium 27 (2000) 97–106.

[31] S. Dargan, I. Parker, Buffer kinetics shape the spatiotemporal patterns of IP3-mediated Ca^{2+} signals, J. Physiol. 553 (2003) 775–788.

[32] M. Falke, On the role of stochastic channel behavior in intracellular Ca^{2+} dynamics, Biophys. J. 84 (2003) 42–56.